SAR Sea-Ice Image Analysis Based on Iterative Region Growing Using Semantics

Qiyao Yu and David A. Clausi, *Senior Member, IEEE*

***Abstract*—Synthetic aperture radar (SAR) has been intensively used for sea-ice monitoring in polar regions. A computer-assisted analysis of SAR sea-ice imagery is extremely difficult due to numerous imaging parameters and environmental factors. This paper presents a system which, with some limited information provided, is able to perform an automated segmentation and classification for the SAR sea-ice imagery. In the system, both the segmentation and classification processes are based on a Markov random-field theory and are formulated in a joint manner under the Bayesian framework. Solutions to the formulation are obtained by a region-growing technique which keeps refining the segmentation and producing semantic class labels at the same time in an iterative manner. The algorithm is a general-segmentation approach named iterative region growing using semantics, which, in this paper, is dedicated to the problem of classifying the operational SAR sea-ice imagery provided by the Canadian Ice Service (CIS). The classified image results have been validated by the CIS personnel, and the resulting classifications are quite successful using the same algorithm applied to diverse data sets.**

***Index Terms*—Expert system, image segmentation, Markov random field (MRF), region growing, sea ice, synthetic aperture radar (SAR).**

I. Introduction

SYNTHETIC aperture radar (SAR) has been intensively used for sea-ice monitoring in polar regions and has been found to have important applications in both scientific and operational activities such as climatic research and ship navigation. In the Canadian Ice Service (CIS), daily ice charts are produced based primarily on RADARSAT-1 SAR sea-ice images. Other sources for producing daily ice charts include ERS-2, NOAA_AVHRR, SSM/I & OLS, QuikSCAT, and previous-day ice charts. Ice charts are sent to coast guards and merchant ships for route planning in sea-ice-infested regions. In producing an ice chart, ice analysts decompose the image into polygon regions, with each polygon representing a visually homogeneous area in the SAR image. A symbol called the egg code, defined by the World Meteorology Organization (WMO) [1], is then assigned to each polygon region, summarizing the information about the type, concentration, and floe size of each ice type existing inside the region. Operationally, this analysis is done manually, and it is limited in throughput, has human bias, and does not classify at a pixel-level resolution.

Computer-assisted analysis is thus desired, the goal of which is to properly segment the image into homogeneous regions and to classify each segmented region with the correct ice type in an automated manner. This will generate an ice map where each pixel is assigned a particular ice type. Unfortunately, significant variations exist with respect to the tone (intensity) and texture appearance of the SAR sea ice due to the complexity of environmental factors and the backscattering and interaction of electromagnetic radiation with the sea ice. Moreover, the existence of notorious speckle noise adds considerable difficulty in extracting the real tone and texture features of the SAR sea ice. The task is thus extremely challenging with respect to both segmentation and classification.

The success of a SAR sea-ice analysis system is thus largely dependent upon its adaptivity to the variable tones and textures of the SAR sea ice. On the other hand, models that are relatively insensitive to the tones and textures are needed for robust descriptions of the ice types. The two issues are associated with the two processes, respectively: the low-level unsupervised segmentation on image pixels and the high-level supervised classification on segmented regions. In the latter, features other than the tone and texture need to be efficiently incorporated, as suggested by the success of human operators in discriminating the ice types using additional high-level knowledge such as floe shape and existence of fractures. Computing such features requires the low-level segmentation to produce correct regions neither oversegmented nor undersegmented. Such a balance is difficult to achieve due to the complexity of the sea-ice scenes, and hence, guidance by the high-level supervised classification is desirable for the low-level-segmentation process.

Such a bidirectional relationship between the segmentation and classification has not been explored before in the SAR sea-ice field. Except for a number of supervised studies [2]–[7] that directly assign each pixel with an ice-type label, most existing publications [8]–[11] deal only with the segmentation task without considering further classification of the segmented regions. As such, the features utilized in all those methods are limited to tone and texture. Some systems [12]–[15] have integrated a classification process but in a postprocessing manner that does not allow the segmentation process to benefit from the incorporation of various high-level features in the classification process.

This paper aims at designing a computer-based analysis system in support of the CIS operations. The system, with the egg code provided, performs an automated joint segmentation and classification of the corresponding polygon region in RADARSAT-1 sea-ice images. Both the segmentation and classification processes in the system are based on the Markov

Manuscript received December 14, 2006; revised June 9, 2007. This work was supported in part by the Natural Sciences and Engineering Research Center Network of Centres of Excellence (NCE) called Geomatics for Informed Decisions (GEOIDE), by the Canadian Ice Service (CIS), and by the CRYospheric SYStem (CRYSYS) in Canada.

Q. Yu is with Eutrovision Inc., Shanghai 200030, China (e-mail: qiyao.yu@eutrovision.com).

D. A. Clausi is with the Department of Systems Design Engineering, University of Waterloo, Waterloo, ON N2L 3G1, Canada (e-mail: dclausi@engmail.uwaterloo.ca).

Digital Object Identifier 10.1109/TGRS.2007.908876

TABLE I
ICE CATEGORIES DEFINED BY WMO [1]

New Ice:	A general term for recently formed ice. These types of ice are composed of ice crystals which are only weakly frozen together (if at all) and have a definite form only while they are afloat.
Grey:	Young ice 10-15 cm thick.
Grey-white:	Young ice 15-30 cm thick.
Thin first-year:	First-year ice of not more than one winter's growth, 30-70 cm thick.
Medium first-year:	First-year, ice 70-120 cm thick.
Thick first-year:	First-year ice over 120 cm thick.
Old Ice:	Ice which has survived at least one summer melt. Often sub-divided into either second year ice or multi-year ice.

random-field (MRF) theory [16] and are formulated in a joint manner under the Bayesian framework. A solution to the formulation is obtained by a region-growing technique which keeps refining the segmentation and producing semantic class labels at the same time in an iterative manner. The algorithm is named iterative region growing using semantics (IRGS) [17]. Novel methods to include domain-specific knowledge are developed, integrated, and applied, and also, the features are efficiently combined to produce successful segmentation and classification of the SAR sea-ice imagery.

In the analysis process, the egg code is provided to the system, giving information about the number of classes and the associated ice types. As such, the system is not fully automated. However, the egg-code information significantly reduces the solution space and is beneficial to the reliability of the system. We currently deem this semiautomated analysis process to be more robust and, hence, more practical than the fully automated ones. The IRGS outputs pixel-based maps that are impractical for the CIS analysts to produce, and such a product would be a meaningful progress for CIS operations [14].

The next section gives a background of the SAR sea-ice analysis research. The IRGS method is then described in Section III and applied to the SAR sea ice in Section IV. Section V presents the experiments and discussions. Section VI presents the summary and future work.

II. BACKGROUND

A. Sea-Ice Types and Chart

Sea ice is generally a mixture of freshwater ice, brine, and air. Based primarily on the age and thickness of the ice, sea-ice types are defined by WMO [1] and are summarized in Table I. Regional ice conditions are then represented by an ice chart. In an ice chart, each outlined region is associated with an egg code which is an oval-shape symbol that contains numerical information about the type, concentration (percentage of area coverage), and floe size of each ice type existing in the specified region. A detailed description can be found at the CIS website [18]. Digitized ice charts have also been used as input to the SAR classification in [19].

B. SAR Sea-Ice Backscatters

A satellite SAR system is able to provide a continuous and regular imaging of the ice-field-overextended areas and, hence, has become a very important tool for sea-ice monitoring in many ice services around the world (i.e., Canada, U.S., and Northern Europe). For example, the primary source for sea-ice analysis in the CIS is the RADARSAT-1 ScanSAR Wide mode data acquired using a SAR instrument operating at C-band (5.3-GHz 5.6-cm wavelength) with HH polarization. The images have a swath of 500 km and have a resolution of 100 m, providing a large and yet sufficiently detailed coverage of vast ocean expanses.

The SAR backscatter is mainly dependent on two factors: the electrical property of the target ice and the roughness of the ice surface [20]. The two factors are the functions of numerous environmental variables including temperature, salinity, wind condition, ocean currents, rate of freezing, history of melting, existence of snow cover, and intrusion of sea water. Measurement of the surface roughness is also greatly influenced by the wavelength, polarization, and incidence angle of the transmitted signal [21]. Modeling of the SAR backscatters of sea ice is thus extremely difficult and becomes even more complex with the existence of speckle noise. There are many speckle-noise filters [22]–[26] in the research literature, but the filtering would possibly break down the texture details and blur the ice-region boundaries. Methods for alleviating incidence-angle fading effects have also been studied [27], but this is an unresolved problem since the fading effect on the backscatter is a function of the ice type.

C. Review of SAR Sea-Ice Analysis

Early research on computer-assisted SAR sea-ice analysis focused on the study of tone and texture features. Mostly in a supervised manner, these efforts compared the SAR sea-ice tone and texture, and generally investigated the different parameters and statistics of gray-level cooccurrence matrix (GLCM) textures [2], [3], [6], [7], [28], [29]. Some more recent papers use unsupervised segmentation techniques as they can theoretically adapt to the varying backscatters of the SAR sea-ice imagery more effectively. Soh and Tsatsoulis [11] applied a dynamic-thresholding and spatial-clustering algorithm to the SAR sea-ice tone. Samadani [10] modeled the tone with a mixture of gamma distributions. Clausi and Yue [8] performed clustering on GLCM and MRF texture features. Karvonen [12] developed a system based on a pulse-coupled neural network. Soh *et al.* [15] chose a watershed and region growing for the segmentation part of a complete analysis system named ARKTOS. Deng and Clausi [9] implemented an MRF model to account for the spatial relationship among pixels for producing segmentation results less sensitive to the SAR speckle noise. Yang *et al.* [30] applied a region-based MRF to polarimetric SAR sea-ice data.

Such research does not typically deal with the classification, namely, the assignment of segmented regions to specific ice-type labels. The classification task, as it is domain-specific, often requires the integration of numerous domain expert knowledge and involves the design of an expert system. Various expert systems, knowledge-based [31]–[34] or probabilistic-based [35], [36], can be found in the literature for different applications, and one relevant work to SAR sea ice is the ARKTOS system [15]. The ARKTOS system generates facts based on the attributes computed from the segmented regions and uses the Dempster–Shafter theory for the inference of

facts. The map-guided MAGSIC [14] is another SAR sea-ice classification system, which accumulates evidence for ice typing by exploring a correlated information between the egg-code regions in the ice chart. MAGSIC uses [9] to segment each polygon SAR region.

III. Iterative Region Growing Using Semantics (IRGS)

Traditionally, the segmentation and classification (if any) are performed separately, with the classification as a postprocessing of the segmentation. A substantial deficiency of such a simple unidirectional link between the two processes is the fact that the segmented regions may not match the real objects well enough for an accurate subsequent classification. In fact, segmentation is generally not a stand-alone problem, but ill-posed if not associated with some constraints, which can be defined from an implicit or explicit interpretation (classification). Therefore, the classification needs to be able to guide the segmentation, and hence, a bidirectional relationship between the two is desired.

The applied method here is called the IRGS and is based on [17]. A more extensive description of the segmentation-only component is presented in a chapter by Yu [37]. The method is characterized by a gradually increased edge penalty (with the difference of penalty between weak and strong edges being gradually reduced) in the objective function and a region-growing segmentation controllable by a labeling process. We extend such a general-segmentation method to the SAR sea-ice analysis by integrating a SAR sea-ice specific classification into the labeling process and by building a bidirectional relationship between segmentation and classification. The system thus allows the segmentation to benefit from the incorporation of various high-level features, such as the shape of ice floes and existence of fractures, which have been important in the operational human analysis of SAR sea-ice images. In this section, the segmentation component is described, and in Section IV, the classification, as it pertains to the SAR sea-ice imagery, is also described.

A. Markov Random Field (MRF)

The MRF [16] provides a method of modeling the joint probability distribution of the image sites in terms of local spatial interactions. In an MRF, each site $s \in S$ is related to others via a neighborhood system η_s. A random field $\mathbf{X}$ is an MRF on S with respect to the neighborhood system η_s if and only if

$$P(\mathbf{X}=\mathbf{x})>0 \qquad \forall \mathbf{x} \in \mathcal{X}$$
$$P(x_s|x_{S-\eta_s}) = P(x_s|x_{\eta_s}) \tag{1}$$

where $\mathcal{X}$ is the configuration space of random field $\mathbf{X}$. By the Hammersley–Clifford theorem [38]

$$P(\mathbf{X}=\mathbf{x}) = \frac{1}{Z}\exp\{-E(\mathbf{x})\} = \frac{1}{Z}\exp\left\{-\sum_{c\in\mathcal{C}} V_c(\mathbf{x})\right\} \tag{2}$$

where $\mathcal{C}$ is the set of cliques which are defined as the sets of mutually neighboring sites, $V_c(\mathbf{x})$ is the energy of configuration $\mathbf{x}$ on clique c, $E(\mathbf{x})$ is the total energy of configuration $\mathbf{x}$, and Z is the normalizing constant. The clique-energy functions model the interactions among pixels in a neighborhood. By defining different forms of clique-energy functions, various MRFs are designed.

The image-segmentation task can be formulated as a maximum *a posteriori* problem in which maximizing the *a posteriori* $P(\mathbf{x}|\mathbf{y})$ gives a solution. Here, $\mathbf{y}=\{y_s|s\in S\}$ represents all pixel values on the image lattice S, and $\mathbf{x}=\{x_s|s\in S\}$ represents the class labels on S. By the Bayes' rule, this is equivalent to maximizing $p(\mathbf{y}|\mathbf{x})P(\mathbf{x})$ in which the prior $P(\mathbf{x})$ is typically modeled by an MRF [9], [16], [39], [40] to incorporate a spatial-context information. For this purpose, a multilevel logistic (MLL) model has been popular [39] whose clique energy is defined as

$$V(x_s,x_t) = \begin{cases} \beta, & \text{if } x_s \neq x_t \\ 0, & \text{otherwise} \end{cases} \tag{3}$$

where s and t are the neighboring sites forming a pair-site clique, and β is a positive number. With such a model, the prior $P(\mathbf{x})$ is large if a local neighborhood region is dominated by one single class and small, otherwise.

Based on the assumption that the value y_s of each pixel s is a constant gray level (related to the corresponding class label x_s) corrupted by an additive independent noise, a Gaussian feature model can be used to give an analytical expression of $p(\mathbf{y}|\mathbf{x})$. The formulation of the segmentation task then becomes

$$\mathbf{X} = \arg\min_{\{x_s, s\in\mathcal{S}\}} \left\{ \sum_{s\in\mathcal{S}} \left\{ \frac{1}{2}\ln\left(2\pi\sigma_{x_s}^2\right) + \frac{(y_s-\mu_{x_s})^2}{2\sigma_{x_s}^2} \right\} + \beta \sum_{\langle s,t\rangle\in\mathcal{C}} \{1-\delta(x_s-x_t)\} \right\} \tag{4}$$

where μ_{x_s} and $\sigma_{x_s}^2$ are the mean and variance of all pixel values in class x_s, and $\delta(\cdot)$ is the Kronecker delta function.

B. Incorporating Edge Strength

The traditional MRF segmentation model is initiated by assuming that each pixel has a random label assigned to it. Here, a region adjacency graph (RAG) is employed [16] to save computation time to assist proper initialization that helps to lead to a globally optimal solution and because region statistics are less sensitive to outliers. A watershed algorithm [41] is run to generate a preliminary oversegmented system, and the RAG is built using the watershed result. Each node in the RAG represents a region (an independent spatial grouping of pixels), and each link represents the common boundary between the regions. The edge strength between for each adjacent region pair is used in the segmentation and classification approaches.

Applying a greater penalty to weak edge and a lesser penalty to strong edge is possible instead of penalizing equally for all boundary-site pairs as in (4). With a penalty function defined as

$$g(\nabla_{st}) = g(|y_s - y_t|) = e^{-(|y_s-y_t|/K)^2} \tag{5}$$

the IRGS method uses a sequence of objective functions in (6) (with K increasing) to approach to the segmentation formulation of (4) from the standard Gaussian mixture problem

$$\mathbf{X} = \arg \min_{\{x_s, s\in\mathcal{S}\}} \left\{ \sum_{s\in\mathcal{S}} \left\{ \frac{1}{2} \ln\left(2\pi\sigma_{x_s}^2\right) + \frac{(y_s - \mu_{x_s})^2}{2\sigma_{x_s}^2} \right\} + \beta \sum_{\langle s,t\rangle\in\mathcal{C}} \left\{ (1 - \delta(x_s - x_t))\, g(\nabla_{st}) \right\} \right\}. \quad (6)$$

The IRGS segmentation is an iterative process. At each iteration, the solution to the objective function (6) for a given K is obtained by a region-merging process and a region-based labeling. The merging criterion is [17]

$$\delta E = \sum_{s\in\Omega_k} \ln(\sigma_k) - \sum_{s\in\Omega_i} \ln(\sigma_i) - \sum_{s\in\Omega_j} \ln(\sigma_j) - \beta \sum_{\substack{s\in\partial\Omega_i \\ t\in\partial\Omega_j, t\in\eta_s}} g\left(|y_t - y_s|\right) \quad (7)$$

where Ω_i and Ω_j are the two regions, $\Omega_k = \Omega_i \bigcup \Omega_j$, and $\partial\Omega_i$ is the set of boundary sites of Ω_i (i.e., $\exists t \in \eta_s, x_s \neq x_t$). If δE gives a negative value, Ω_i and Ω_j can be merged, and if δE produces a positive value, Ω_i and Ω_j will not be merged. When the region-merging process is completed (i.e., no remaining region pairs satisfy the merging criterion), a RAG [16] can be updated from the obtained regions. An MRF based on the RAG is used to model the region-based labeling process, and the corresponding single-node clique-energy function is

$$V_1(x_i) = \sum_{s\in\Omega_i} \left\{ \frac{1}{2} \ln\left(2\pi\sigma_{x_i}^2\right) + \frac{(y_s - \mu_{x_i})^2}{2\sigma_{x_i}^2} \right\} \quad (8)$$

and the pair-node clique energy is

$$V_2(x_i, x_j) = \begin{cases} \beta \sum_{\substack{s\in\partial\Omega_i \\ t\in\partial\Omega_j, t\in\eta_s}} g\left(|y_t - y_s|\right), & \text{if } x_i \neq x_j \\ 0, & \text{otherwise} \end{cases} \quad (9)$$

where x_i is the label of region Ω_i. Finding the global minimum of the summation of the above energies over the entire RAG, which is exactly (6), gives a labeling for the current iteration. A greedy combinatorial optimization process is applied.

C. IRGS Algorithm

The overall algorithm of IRGS is described in Table II. At first, an initial RAG is built based on a deliberately oversegmented result [41]. Random labels are then assigned to each node, and the iterative process begins with the feature-model parameter estimation based on the current labeling. Region-merging and labeling processes are then performed during each iteration, and when completed, a new iteration begins with an increased edge penalty. The iterations continue until a maximum number of iterations[1] have been reached. It should be noted that the two regions Ω_i and Ω_j are not allowed to be merged if they do not have the same label, the purpose of which is to suppress the merging between parts of different objects that have weak boundaries in between. This concept is known as semantic region growing [42], [43], and similar ideas also exist [44]. Here, the merging and labeling are iterative and, as such, is referred to as IRGS. Although the labeling process modeled by (8) and (9) has no semantic meanings, it is possible to replace it with a domain-specific labeling process and to integrate high-level knowledge. This is presented in the next section.

[1]We set it to 100, and our experiments all converge (no further configuration changes of $\mathbf{x}$) within 80 iterations.

TABLE II
ALGORITHM OF THE GENERAL IRGS SEGMENTATION

1. Construct an initial RAG and assign each node with a random class label. Initially, $K = 0$.
2. Based on the current segmentation result corresponding to the RAG nodes and the class labels, compute the Gaussian feature model parameters for each class.
3. Compute the energy difference δE by (7) for each pair of linked nodes that have a same region label, and find the minimum δE_{min} across all these.
4. If $\delta E_{\min}$ is negative, merge the corresponding two nodes to form a single node and go back to step 3. Otherwise proceed to step 5.
5. Perform the labelling on the new RAG. The process scans each node in a random order, and for each node scanned chooses the label that produces the minimum energy for (6).
6. If a maximum number of iterations has not been completed, increase K and go back to step 2.

IV. IRGS Applied to SAR Sea-Ice Imagery

For the classification of SAR sea ice, the domain knowledge includes tone (intensity), texture, shape, and existence of fractures. Thicker ice generally has brighter tones than thinner ice types within the same image, but such a tendency is not reliable due to the influence of factors such as snow cover, surface roughness, and incidence variations.

Texture has the potential to be relatively insensitive to incidence variations and has attracted most of the attention in the SAR sea-ice community. Two kinds of textures, microtexture and macrotexture, are possible for ice identification. An example is shown in Fig. 2(a). Here, the water and land areas are found predominantly in the bottom middle of the scene. Regions that are relatively dark, containing brighter lines (ice ridges caused by pressure), are gray–white ice, and the rest of the regions represent gray ice. The gray ice has noticeable coarser microtextures, whereas the gray–white ice is characterized by macrotextures formed by dark floes and bright ridges. However, microtextures are often masked by speckle noise, and macrotextures are heavily scale-dependent. Descriptive (with respect to ice types) and reliable features are difficult to extract for both kinds of textures. In this paper, texture is not considered.

A more robust feature used extensively by ice analysts is the floe shape. Thicker ice typically has well-defined elliptical floes. For example, as shown in Fig. 4(a), it is dominated by two ice types (medium first year and thick first year). The thick first-year ice, although thicker than the other, is relatively dark. The identification of thick first-year ice thus cannot be based on the tone feature but on the existence of well-defined floes.

Existence of fractures is another possible feature. Although it is not definite that the occurrence of fractures indicates thinner ice types, thin ice types such as gray and gray–white are often observed to have leads (long narrow fractures that ships can navigate through). In Fig. 2(a), dominant leads are clearly visible in the thinner gray-ice region.

In this section, the above domain-specific knowledge is incorporated in the labeling steps of the IRGS process also by means of clique-energy functions. In addition to the general-segmentation clique functions (8) and (9), new clique functions are designed to give decreased values if the corresponding classification of the regions tends to be consistent with the measurements and domain knowledge [35].

A. Tone

The simplest unary property of a segmented region is the mean of the tone. However, tone is sensitive to environmental factors and imaging parameters. The SAR backscatter for various ice types has high intraclass variance, making distinction based on the absolute backscatter not possible. We have noticed, however, that there is more useful information based on the relative difference of tone rather than the absolute value, and hence, this information is more appropriately represented by a pair-node clique function rather than a single-node clique-energy function. The negative logarithm of the distribution of the tone difference is a reasonable choice for the form of the corresponding clique-energy function. However, this requires extensive training which is limited by the availability of ground truth data. A much simpler clique function is used here, namely

$$V_2^{(\mathrm{td})}(x_i, x_j) = \begin{cases} L_{ij}C^{(\mathrm{td})}, & x_i \text{ is thicker ice, } y_i^{(\mathrm{td})} < y_j^{(\mathrm{td})} \\ L_{ij}C^{(\mathrm{td})}, & x_j \text{ is thicker ice, } y_i^{(\mathrm{td})} > y_j^{(\mathrm{td})} \\ 0, & \text{otherwise} \end{cases} \quad (10)$$

where $y_i^{(\mathrm{td})}$ is the mean tone of region Ω_i, and $C^{(\mathrm{td})}$ is a positive number experimentally set. L_{ij} is the length of the boundary between regions Ω_i and Ω_j and is included in this clique-energy function based on the intuition that the importance of a binary relation between two neighboring regions should be related to their common boundary length. Therefore, all pair-node clique-energy functions are weighted by this common boundary length. Similarly, the importance of a region is related to its size, and thus, all later-presented single-node clique energies are weighted by the region size (N_i).

B. Shape

Two shape features are used. The first shape feature identifies elongated shapes and is used to describe leads. The lead-shape feature is measured by $y^{(\mathrm{ld})} = l_{\mathrm{cross}}/l_{\max}$, where $l_{\max}$ is the long side of the minimum bounding rectangle, and l_{cross} is the minimum crossing length of the segmented region in the direction normal to the long axis of the rectangle. These are shown in Fig. 1. A detailed computation formula for the bounding rectangle can be found in [15]. Within the range [0, 1], $y^{(\mathrm{ld})}$ has a low value if elongated and a high value when not

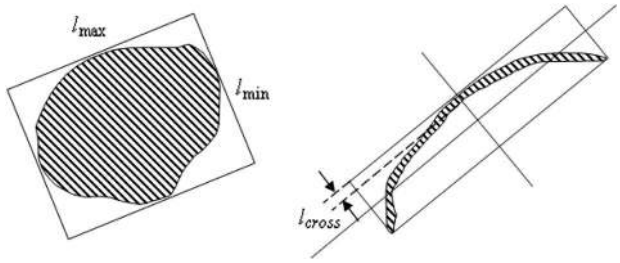

Fig. 1. Minimum bounding rectangle and shape parameters.

elongated. Based on this feature and certain threshold $C_2^{(\mathrm{ld})}$, it is then possible to determine whether the shape is elongated. We make the corresponding clique-energy function soft and define it as in (11). Here, N_i is the number of pixels contained in region Ω_i, and $C_1^{(\mathrm{ld})}$ is the range (or weight) associated with this clique energy

$$V_1^{(\mathrm{ld})}(x_i) = \begin{cases} N_i C_1^{(\mathrm{ld})} \left[\dfrac{\left(\frac{y_i^{(\mathrm{ld})}}{C_2^{(\mathrm{ld})}}\right)^2}{1+\left(\frac{y_i^{(\mathrm{ld})}}{C_2^{(\mathrm{ld})}}\right)^2} - \frac{1}{2} \right], & \text{is lead} \\ 0, & \text{otherwise.} \end{cases} \quad (11)$$

The other shape feature is a measure of the fit of a region to an elliptical shape. For each segmented region, a simple ellipse-fitting algorithm is first applied. Suppose that the orientation of the computed bounding rectangle (the angle between the long axis and the horizontal direction) is denoted by θ. The long axis a and short axis b of the ellipse are, respectively

$$a = 2\sqrt{u_{20}\cos\theta^2 + 2u_{11}\sin\theta\cos\theta + u_{02}\sin\theta^2} \quad (12)$$

$$b = 2\sqrt{u_{20}\sin\theta^2 - 2u_{11}\sin\theta\cos\theta + u_{02}\cos\theta^2} \quad (13)$$

where u_{20}, u_{11}, and u_{02} are the typical second-order moments of the segmented region [45]. The center of the ellipse is set as the centroid of the region. It is then straightforward to compute for each region Ω_i the ellipse-fitting error with respect to the boundary sites $\partial\Omega_i$ as

$$y_i^{(\mathrm{el})} = \frac{\sum_{s\in\partial\Omega_i} D(s, \mathbf{e}_i)}{\int_{s\in\partial\Omega_i} ds} \quad (14)$$

where $D(s, \mathbf{e}_i)$ is the Euclidean distance between the boundary site s and the nearest site of ellipse $\mathbf{e}_i$.

We then hypothesize that, for the image being analyzed, one or more ice types are characterized by ellipse-shape floes that make them different from other types (including water if there is) existing in the image. This hypothesis is tested by binary (floe versus nonfloe) clustering and a thresholding on the resulting Fisher criterion J [46]. The corresponding clique energy is defined as follows:

$$V_1^{(\mathrm{el})}(x_i) = \begin{cases} -N_i O_{x_i} C_1^{(\mathrm{el})}, & \text{is floe and } J > C_2^{(\mathrm{el})} \\ 0, & \text{otherwise} \end{cases} \quad (15)$$

where N_i is the number of pixels of region Ω_i, $C_1^{(\mathrm{el})}$ is a positive number, and $C_2^{(\mathrm{el})}$ is the threshold in determining whether the

TABLE III
FLOE VERSUS-NONFLOE CLUSTERING

1.	Group regions of the same class label (obtained from the previous classification process) into the same cluster. Thus, several region clusters are obtained.
2.	Further group the obtained region clusters into two - floe and non-floe. Exhaustively try different possibilities of such grouping, and compute the corresponding Fisher criteria J.
3.	Select the largest J and the corresponding linear discriminant.

hypothesis is true for the current image. Here

$$O_{x_i} = |\{x_j | \text{Thick}(x_j) < \text{Thick}(x_i), x_j \in T\}| \tag{16}$$

where $\text{Thick}(x_i)$ is the thickness of ice type x_i, T is the set of possible ice types in the current image (given by the egg code), and $|\cdot|$ denotes cardinality. That is, O_{x_i} gives the order of the ice type x_i by increasing the thickness among all ice types existing in the current image. This function gives a decreased energy for floe regions belonging to thicker ice types subject to the existence of the two-cluster (floe versus nonfloe) problem, which is to make sure that the current image does have both floe and nonfloe regions, and hence, the incorporation of ellipse-shape information is helpful.

Two features are involved in the two-cluster problem. Besides the ellipse-fitting error $y_i^{(\text{el})}$, the average boundary strength $y_i^{(\text{bs})}$ is also introduced and computed as the average of gradient magnitude along the region boundary $\partial\Omega_i$. These two features jointly describe a well-defined floe. The clustering process is described in Table III. The Fisher criterion J obtained at the third step in the table is then used in (15), and the corresponding linear discriminant is used for further clustering of individual regions into floe and nonfloe types.

The most common reason for the failure of shape-based analysis methods is the fact that image segmentation often generates either oversegmented or undersegmented region that does not match well with the real objects. It is thus important to make sure that the above clustering is performed on the right scale so that such a floe-versus-nonfloe discrimination is valid and efficient. Fortunately, the IRGS produces intermediate results of different scales, and hence, it is theoretically possible to select and preserve good results during the iterations. As shown later in Section IV-D, the incorporation of domain-specific classification into the IRGS process causes a new overall objective functions other than the original (6), and the resulting merging criterion inhibits the undersegmentation phenomenon caused by merging between floes.

C. Cooccurrence of Classes

The cooccurrence of classes is another important binary relationship. Although generally applicable, in this paper, such cooccurrence information is for describing the existence of leads in ice floes only. The system considers the lead as a separate class and incorporates the cooccurrence knowledge into a pair-node clique energy as follows:

$$V_2^{(\text{co})}(x_i, x_j) = \begin{cases} -L_{ij}\hat{O}_{x_j}C^{(\text{co})}, & x_i \neq x_j, x_i \text{ is lead} \\ -L_{ij}\hat{O}_{x_i}C^{(\text{co})}, & x_i \neq x_j, x_j \text{ is lead} \\ 0, & \text{otherwise} \end{cases} \tag{17}$$

where $C^{(\text{co})}$ is a positive number, L_{ij} is the length of the boundary between the regions Ω_i and Ω_j, as indicated by (10), and $\hat{O}_{x_i}$ is the order of the ice type x_i by decreasing the thickness among all ice types (excluding new ice) existing in the current image.

D. Overall Energy and Optimization

The overall energy of the SAR sea-ice analysis system is

$$E = E_{\text{low}} + E_{\text{high}} \tag{18}$$

where

$$E_{\text{low}} = \sum_{s\in\mathcal{S}} \left\{ \frac{1}{2}\ln\left(2\pi\sigma_{x_s}^2\right) + \frac{(y_s - \mu_{x_s})^2}{2\sigma_{x_s}^2} \right\} + \beta \sum_{\langle s,t\rangle\in\mathcal{C}} \{(1-\delta(x_s - x_t))\, g(\nabla_{st})\} \tag{19}$$

is the energy related to low-level segmentation as per (6) and

$$E_{\text{high}} = \sum_{i\in\mathcal{G}} \left\{ V_1^{(\text{ld})}(x_i) + V_1^{(\text{el})}(x_i) \right\} + \sum_{\langle i,j\rangle\in\mathcal{E}} \left\{ V_2^{(\text{td})}(x_i, x_j) + V_2^{(\text{co})}(x_i, x_j) \right\} \tag{20}$$

is the energy related to the high-level classification. In (20), $\mathcal{G}$ is the RAG, and $\mathcal{E}$ is the set of cliques defined over the edges in the graph (i.e., a pair of sites $\langle i, j\rangle$ forms a clique if i and j are connected by an edge).

The computation of E_{high} involves the region size N_i and the boundary length L_{ij}, as per (10), (11), (15), and (17). The introduction of N_i and L_{ij} makes E_{high} scale proportionally with E_{low} for images of different resolutions. Also, the lead-shape feature $y^{(\text{ld})}$ is scale invariant as it is a ratio, and the ellipse-shape feature $y^{(\text{el})}$ is only used in the floe-versus-nonfloe clustering without introducing any resolution sensitivity to the overall objective energy function.

As in the general IRGS algorithm in Table II, the optimization consists of two cooperative processes: the region merging for segmentation and the region-based labeling for classification. For SAR sea ice, both processes aim to reduce the overall energy in (18). The merging criterion of (7) is changed to

$$\delta E = \sum_{s\in\Omega_k} \ln(\sigma_k) + V_1^{(\text{ld})}(x_k) + V_1^{(\text{el})}(x_k) - \sum_{s\in\Omega_i} \ln(\sigma_i) - \sum_{s\in\Omega_j} \ln(\sigma_j) - \beta \sum_{\substack{s\in\partial\Omega_i \\ t\in\partial\Omega_j, t\in\eta_s}} g\left(|y_t - y_s|\right) - V_1^{(\text{ld})}(x_i) - V_1^{(\text{el})}(x_i) - V_1^{(\text{ld})}(x_j) - V_1^{(\text{el})}(x_j) \tag{21}$$

and the labeling process updates for each region i the class label x_i, which satisfies the following equation:

$$\mathbf{X} = \arg\min_{x_i} \left\{ V_1(x_i) + V_1^{(\text{ld})}(x_i) + V_1^{(\text{el})}(x_i) + \sum_{\langle i,j\rangle\in\mathcal{E}} \times \left\{ V_2(x_i, x_j) + V_2^{(\text{td})}(x_i, x_j) + V_2^{(\text{co})}(x_i, x_j) \right\} \right\} \tag{22}$$

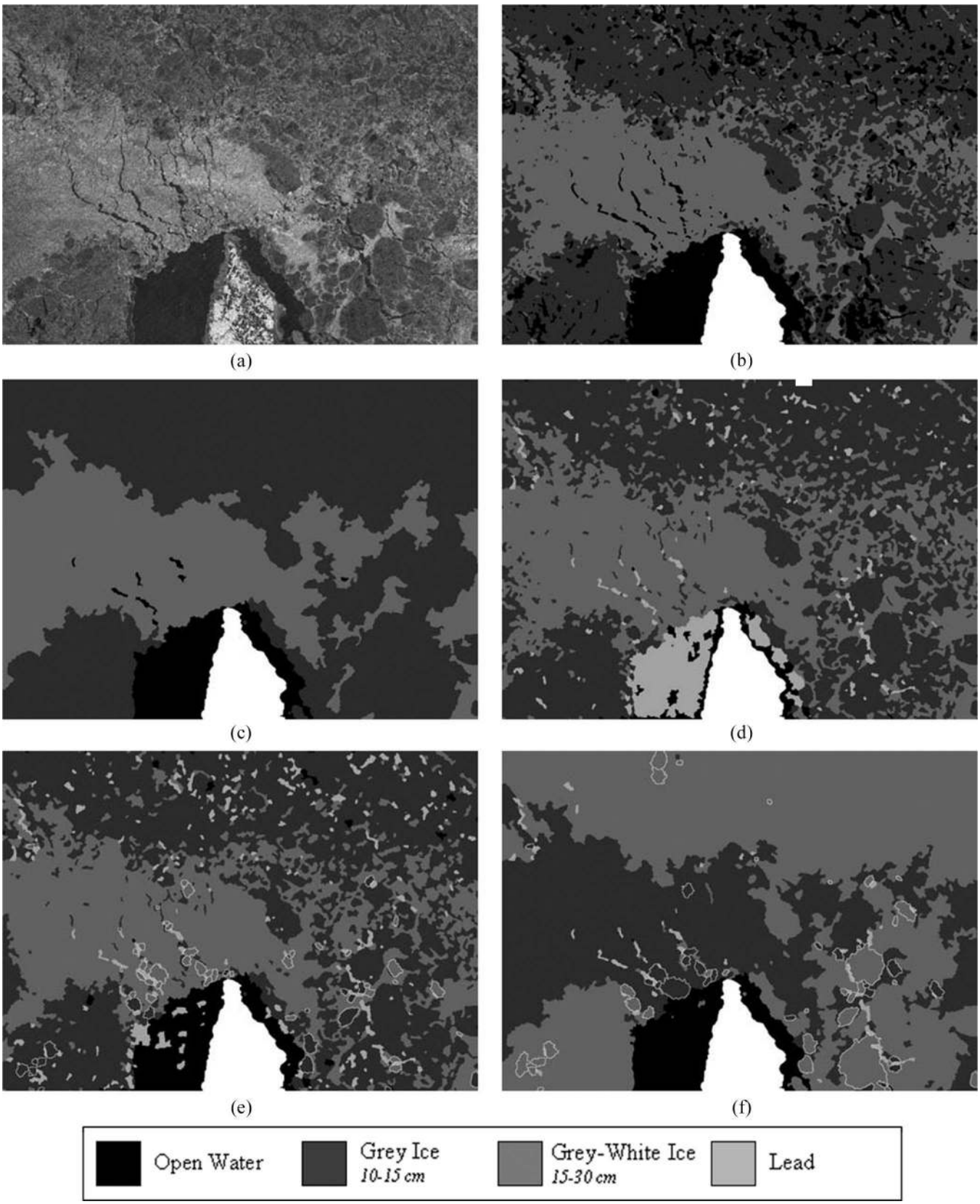

Fig. 2. Segmentation and classification of a SAR sea-ice image captured over the Gulf of St. Lawrence on February 20, 1998. The image size is 1209 × 865. It has three classes: Water, gray ice, and gray–white ice. (a) Original SAR image. (b) Result using V-MLL. Note that open water is incorrectly identified throughout the gray–white region. (c) IRGS result without the high-level knowledge. Note that the gray and gray–white ice labels are reversed. (d) and (e) IRGS after 8 and 34 iterations. Note that the gray and gray–white ice labels are reversed. (f) IRGS after 77 iterations. Note that, at this point, the gray and gray–white ice labels are now properly assigned to the regions. In (b)–(f), white indicates masked land regions not included in the computation. Bright lines in (e) and (f) outline the boundaries of detected floes. The gray-scale coding of the segmentation in (b) and (c) selects the same four levels used for ice types in (d)–(f) to satisfy visual comparisons.

Compared to (7), the merging criterion of (21) considers the shape of the regions in addition to the regional homogeneity and boundary strength. For example, if both Ω_i and Ω_j are well-defined floes with a moderate length of common boundary, the merging result Ω_k is likely far from the ellipse shape and, hence, is grouped in the nonfloe cluster. The related energy difference

$$V_1^{(\mathrm{el})}(x_k) - V_1^{(\mathrm{el})}(x_i) - V_1^{(\mathrm{el})}(x_j) \tag{23}$$

is relatively high. Thus, this merging operation may be prohibited due to a possible positive energy difference in (21).

The merging is only allowed between regions belonging to the same class and does not change the class label. As such, O_{x_i} in (15) is fixed during the merging operations. Therefore, $V_1^{(\mathrm{el})}$ is only proportional to the region size, no matter which of the two situations in (15) the region belongs to. If all three regions Ω_i, Ω_j, and Ω_k belong to the same one of the two situations in (15), the energy difference in (23) is just zero since the region size of the merging result Ω_k is the sum of those of Ω_i and Ω_j. Thus, the floe-shape information does not play a role in the merging criterion when all the three regions are floes (or nonfloes).

By the same philosophy, the energy difference related to $V_2^{(\mathrm{co})}$ is always zero. Moreover, if the merging does not change the relative brightness between the neighboring regions of difference classes, which is usually the case, the energy difference related to $V_2^{(\mathrm{td})}$ is also zero. This is the reason why both $V_2^{(\mathrm{td})}$ and $V_2^{(\mathrm{co})}$ do not show up in the merging criterion (21).

In the region-based labeling process, we first group the regions into several clusters based on their provisional ice-type labels from previous runs, as in Table III. It is sometimes necessary to change the labels of all regions belonging to the same cluster together rather than change them individually. For example, at the initial stages of the processing in Fig. 2, hundreds of small regions exist in the center of the image corresponding to the relatively brighter gray ice. However, such a cluster of regions is labeled as gray–white ice in the first several runs since the tone-difference knowledge indicates that brighter regions correspond to thicker ice. As the iteration continues, the two-cluster (floe versus nonfloe) hypothesis becomes true at a certain scale. Floe information begins to play a role, making it possible for this cluster of regions to change their labels to gray ice. If the labeling is on individual regions, the process will be extremely slow and may easily be trapped in an inaccurate configuration. Therefore, we first try to minimize the energy on a region cluster base. This is allowed to be an exhaustive search since the number of clusters is not more than five (in addition to water, the egg-code definition allows at most four different ice types). Individual regions are then investigated, and their labels are updated separately.

The overall algorithm is shown in Table IV.

TABLE IV
ALGORITHM OF THE SAR SEA-ICE IRGS ANALYSIS

1. Construct an initial RAG and assign each node with a random class label. Initially, $K = 0$.
2. Based on the current segmentation result corresponding to the RAG nodes and class labels, compute the Gaussian feature model parameters.
3. Compute the energy difference δE by (7) for each pair of linked nodes that have a same region label, and find the minimum δE_{min} across all these.
4. If $\delta E_{\min}$ is negative, merge the corresponding two nodes to form a single node and go back to step 3. Otherwise proceed to step 5.
5. Update the RAG. Group regions of the same label into the same cluster, and hence obtain several region clusters. Compute the J in (15) by performing the operations in Table III.
6. Find the configuration of cluster labels that minimize the energy (18) by exhaustive searching.
7. Refine the labelling on individual regions to minimize (18). The process scans each node in a random order, and for each node scanned chooses the label that produces the minimum energy for (22).
8. If a maximum number of iterations has not been completed, increase K and go back to step 2.

E. Parameters and Adaptive Weighting

The parameters for clique-energy functions are selected by trial and error. Here, the trial range of weights $C^{(\mathrm{td})}$, $C_1^{(\mathrm{ld})}$, $C_1^{(\mathrm{el})}$, and $C^{(\mathrm{co})}$ is set around one ([0.1, 10]) so that the importance of the corresponding clique-energy functions is approximately at the same level as that of the segmentation energy in the overall objective function in (18). The two thresholds $C_2^{(\mathrm{ld})}$ and $C_2^{(\mathrm{el})}$ have physical meanings and are adjusted around intuitively reasonable values. In the trials for each parameter, only the corresponding energy function is used, and all others among (10), (11), (15), and (17) are taken out. Two SAR sea-ice images have been selected for the trials, and the obtained best parameters have been found applicable to all other 17 images tested in our experiments. The parameter values are summarized in Table V. The sensitivity of the overall solution to these parameters is reasonably low since the parameters can be adjusted around the selected values within a moderate range without changing the essence of the final result. For example, the range [0.2, 2] for $C_1^{(\mathrm{el})}$ produces similar results.

TABLE V
SUMMARY OF THE CLIQUE-ENERGY PARAMETERS FOR HIGH-LEVEL CLASSIFICATION

$C^{(td)}$	$C_1^{(ld)}$	$C_2^{(ld)}$	$C_1^{(el)}$	$C_2^{(el)}$	$C^{(co)}$
0.1	0.1	0.3	0.4	0.2	0.3

In practice, we may want to have a variable weighting instead of a constant weighting between the segmentation and classification energy terms [47], or between different expert knowledge. For example, tone information is more reliable than others (e.g., shape) at the early stages of the process when the obtained regions are highly probable to be oversegmented. Therefore, we multiplied the two tone-related clique-energy functions $V_1(\cdot)$ and $V_2^{(\mathrm{td})}(\cdot)$ with a weight, which decreases with increasing iterations, as shown in the following equation:

$$W_{k+1} = 0.9W_k + 0.1 \tag{24}$$

where W_k is the weight for iteration k, and W_0 is an initial value set as 80 in this paper. The weight is lower-limited to one by the equation.

V. Experiments and Discussions

The method is tested on 19 SAR sea-ice images, processed and provided by the CIS, of eight different scenes covering various regions such as Baffin Bay, Gulf of St. Lawrence, and Beaufort Sea, and in various seasons as well. They are all acquired by RADARSAT in ScanSAR C-band mode and have a resolution of 100 m (images of 50-m resolution are 2×2 block-averaged by the CIS). Five examples are included in this paper. Due to the difficulty of obtaining the pixel-level ground truth, the experiment results are evaluated subjectively. An online meeting with experts in the CIS was held on April 26, 2006 for such an evaluation. In addition, a comparison is performed (with respect to the segmentation goal) between the proposed IRGS system and a recent SAR sea-ice segmentation approach [9] named (V-MLL) here, which uses a variable weighting between the feature model and the MLL context model.

The egg code is provided as an input to improve the effectiveness and reliability, as mentioned in Section I. However, the only egg-code information utilized by the system is the ice types existing in the egg-code region. An information of concentration and floe size has been ignored because it is highly subjective. Therefore, the system has only the knowledge of the number and names of ice classes. It is also possible to infer from the ice chart other information, such as a coarse estimate of the tone of a specific ice class, by exploring the correlations between the various egg-code regions of the same ice chart [14]. However, the success of such information extraction depends on the correctness and information richness of the ice chart. This paper deals with the individual egg-code region only.

The first test sample is shown in Fig. 2(a). The corresponding task is a three-class segmentation and classification among water, gray ice, and gray–white ice. The center of the bottom is land, which is excluded from all computations and is represented by white regions in Fig. 2(b)–(f). The dark region surrounding the land is water. Regions having dark ice floes with brighter ridges in between are gray–white ice, and the rest are gray ice. The difficulty of this task lies in both the segmentation and the classification parts. The segmentation is greatly influenced by heavy noise and the large intraclass variations of the gray–white ice, whereas the classification relies on floe and leads information for correct identification of ice types. The V-MLL gives a highly oversegmented result in Fig. 2(b), and many dark gray–white ice floes are mistakenly assigned the same label as the water. The IRGS system gives a satisfactory segmentation result in Fig. 2(f), having achieved a good balance between region consistency and detail preservation. In the result, those bright lines show the boundaries of floes detected during the process. Some leads are too narrow to be accurately captured by the initial watershed and, thus, are lost by subsequent merging processes. Although some floes and segments of leads are missing, the detected floes and leads play an important role in correctly distinguishing between gray ice and gray–white ice.

To demonstrate this, intermediate results have been included in Fig. 2(d) and (e). Early stages of the process produce results of similar level of quality as V-MLL, as shown in Fig. 2(d), if the bright leads in the figure are also considered to be water. Here, the large population of lead labels (even in the water region) is caused by the initial large amount of tiny regions among which some happen to be elongated and dark. Because Fig. 2(d) is too oversegmented (average region size is 149), there is not a distinct cluster of floe regions, and the floe-shape energy (15) is always zero and does not play a role. As a result, the classifications of the segmented regions are mainly based on tone, and the labeling of gray ice and gray–white ice has been mistakenly reversed since the tone energy of (10) always classifies brighter regions with thicker ice types. As more iterations have been completed, tiny regions are merged, and the regions corresponding to floes begin to appear. At iteration 34, some floes are detected, as shown in Fig. 2(e). However, the population of the detected gray–white ice floes is not yet large enough to reverse the labeling of the gray ice and gray–white ice at this stage. As the process continues, more and larger gray–white ice-floe regions are obtained, and more accurate classifications of the segmented regions are possible. The final result in Fig. 2(f) has preserved most floes detected during all the iterations and distinguished correctly between the gray ice and gray–white ice.

The previous paragraph shows how the segmentation influences the classification. On the other hand, the segmentation is also influenced by the classification in the IRGS process. Fig. 2(c) shows the IRGS result without including the high-level knowledge clique functions of (10), (11), (15), and (17). This segmentation result is better than that of the V-MLL in producing large homogeneous regions for gray ice and gray–white ice but is inferior in preserving the lead regions. By comparing Fig. 2(c) and (f), it is clear that an improvement in detail preservations has been achieved by incorporating the high-level knowledge that favors semantic meaningful configurations. For example, a lead and a gray-ice region not observed in Fig. 2(c) appears in the top left of Fig. 2(f) due to the influence of the domain knowledge that favors the elongated shape and dark tone of the lead region and the cooccurrence of gray ice and leads.

For better understanding of the role of various high-level knowledge, different combinations of their clique functions, with others discarded, have been included in the segmentation and classification processes. Fig. 3 shows some examples. In Fig. 3(a), only the elongated-shape energy (11) is included. As the system knows nothing about whether a lead should be bright or dark, many bright ridges are labeled as leads. For the same reason, there is no information for making decisions for other classes, and hence, the other class labels are randomly determined. Compared to Fig. 2(c), more details have been preserved for the bright ridges by chance due to the incorporation of the elongated-shape energy which is designed to describe the lead shape. Knowledge of the cooccurrence of classes is then incorporated in Fig. 3(b) in addition to the elongated-shape energy. This knowledge favors the cooccurrence of leads and the thinner of the two ice types—gray ice. Again, bright ridges are mistakenly identified as leads, as in Fig. 3(a), and the gray–white regions are mistakenly identified as gray since they are neighboring to the identified "leads." Greater preservation of details has been achieved by the incorporation of such knowledge, although the classification is still incorrect. To solve the problem, tone information has to be included, and the corresponding result is shown in Fig. 3(c). The ridges are no longer mistaken as leads, but the labels of gray ice and gray–white ice are reversed. Correction of this reversal

(a)

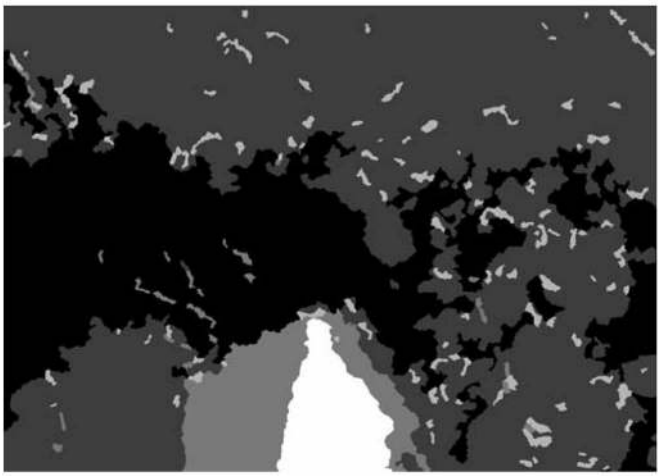

(b)

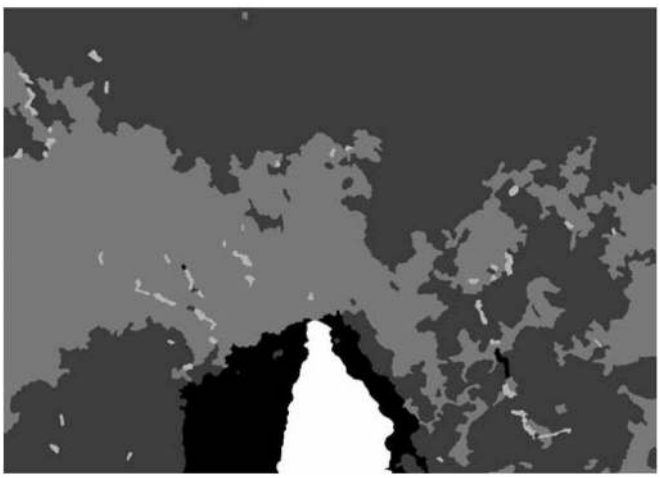

(c)

Fig. 3. Different combinations of high-level knowledge cliques in the segmentation and classification in Fig. 2(a). (a) Only elongated shape (11) included. (b) Elongated shape (11) and cooccurrence of classes (17) included. (c) Elongated shape (11), cooccurrence of classes (17), and tone difference (10) included.

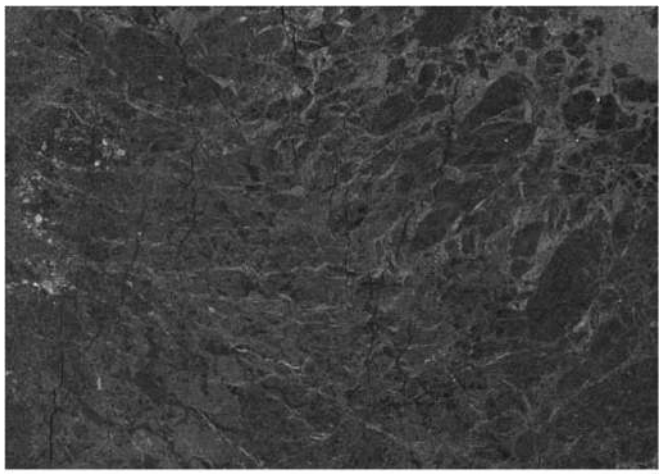

(a)

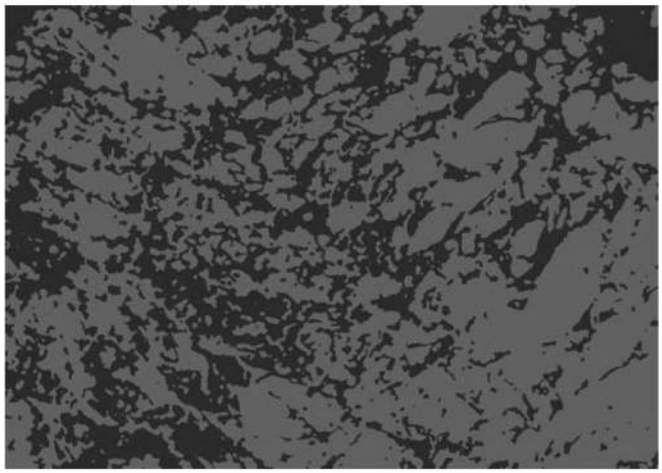

(b)

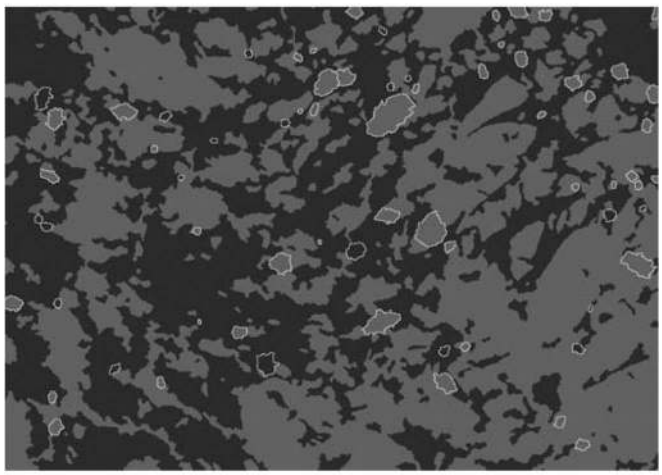

(c)

Fig. 4. Segmentation and classification of a SAR sea-ice image captured over the Baffin Bay on February 7, 1998. The size is 1212×862. It has two classes: medium first-year ice and thick first-year ice. In (c), bright lines outline the boundaries of detected floes. The gray-scale coding of the segmentation in (b) selects the same two levels used for ice types in (c) for visual-comparison need. (a) Original. (b) V-MLL result. (c) IRGS result.

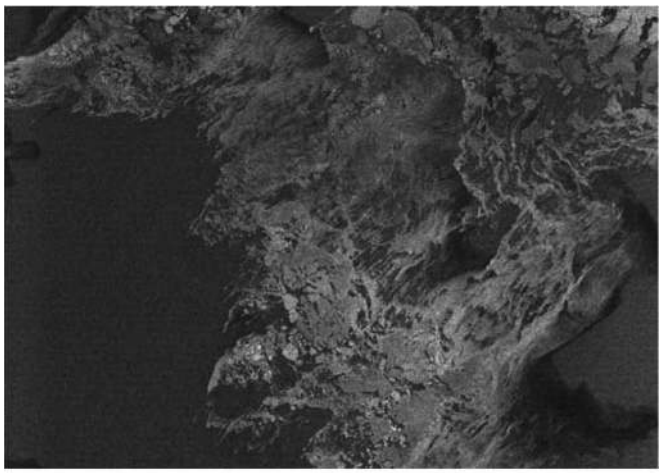

(a)

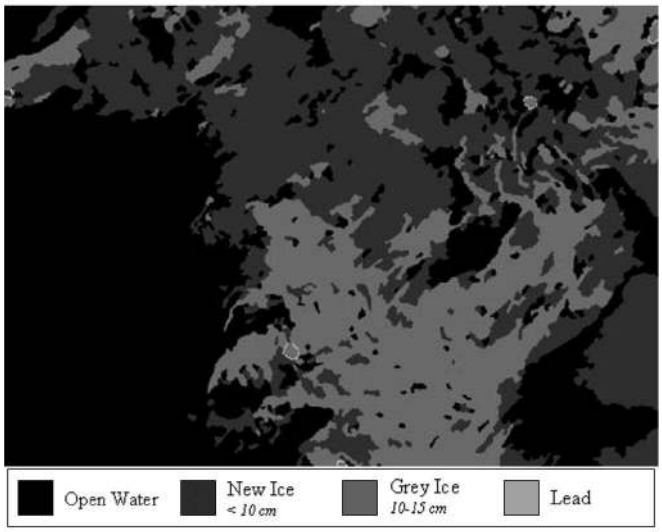

(b)

Fig. 5. Segmentation and classification of a SAR sea-ice image captured over the Beaufort sea on October 13, 1997. The size is 1212 × 860. It has three classes: water, new ice, and gray ice. (a) Original. (b) IRGS result.

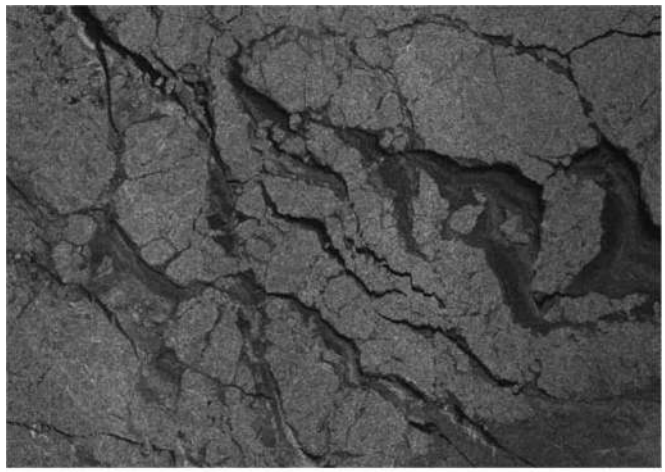

(a)

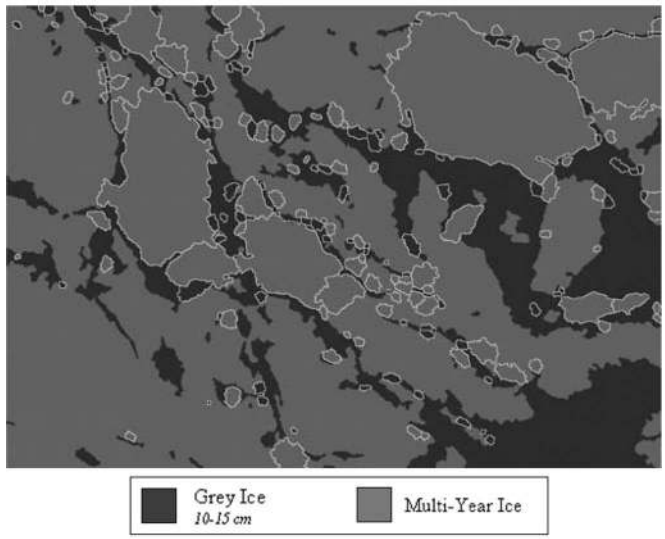

(b)

Fig. 6. Segmentation and classification of a SAR sea-ice image captured over the Beaufort sea on October 13, 1997. The size is 1212 × 856. It has two classes: gray ice and multiyear ice. (a) Original. (b) IRGS result.

requires floe knowledge, as already mentioned in the previous paragraph.

Fig. 4(a) shows another example showing the importance of the floe information. The image consists of two ice types—medium first-year ice and thick first-year ice. The thicker of the two can be identified by dark well-defined floes and dominates the right part of the image. Again, the bright lines in Fig. 4(c) show that some of those floes have been detected and result in the correct discrimination between the two ice types. It can clearly be found that many visually obvious floe regions are not quite elliptic; thus, our ellipse description of the floe shape is not always suitable. For the segmentation quality, the V-MLL in Fig. 4(b) has preserved more details than the IRGS in Fig. 4(c). However, it is difficult to conclude which is better due to the unavailability of the ground truth data.

Fig. 5(a) consists of three classes—water, new ice, and gray ice. In the gray-ice region, in the bottom of the image, there are some small ice floes with gaps in between. The obtained IRGS result in Fig. 5(b) consists of large regions and does not preserve those gaps well. On the other hand, new ice does not have clear boundaries but ambiguous transition regions to water. The quality of the details in the new-ice regions is difficult to evaluate due to the ambiguity of those classes. In the bottom-right corner, the relatively brighter water region (probably caused by wind and incidence-angle effects) is separated from the surrounding darker water and is classified as new ice. Correct identification of this water region probably needs to rely on other features, for example, textures, as the textural appearance of this water region looks quite similar to the large water body in the left of the image. Another possible scheme is to divide the open water into two classes: one rough and one smooth. These concepts are planned as part of future work.

Two other examples are shown in Figs. 7 and 8, respectively. Subjectively, satisfactory segmentations have been obtained, and correct ice identifications are achieved. An error has occurred in the bottom-right corner of Fig. 6, where the multiyear ice is relatively dark due to snow cover and has been mistakenly labeled as gray ice.

Since the IRGS is region-based and the number of regions keeps decreasing by the merging process, the computation

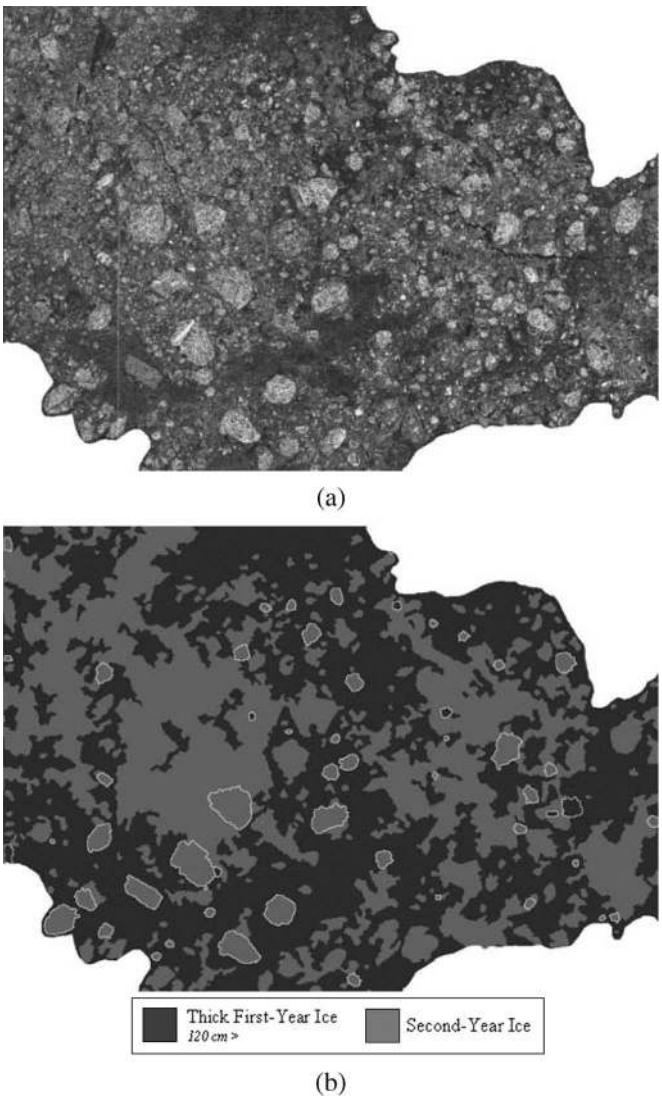

Fig. 7. Segmentation and classification of a SAR sea-ice image captured over the Baffin Bay on February 7, 1998. The size is 1212 × 862. It has two classes: thick first-year ice and second-year ice. The white regions belong to other egg-code regions and are not involved in computation. (a) Original. (b) IRGS result.

speed is much faster than the pixel-based methods such as V-MLL. For the tested images, the average execution time by IRGS is 94 s, whereas that of the V-MLL is 338 s for the same number of iterations on a Toshiba laptop of P3 800 MHz with 128MB RAM. These are both within the range of acceptable classification times in support of operational ice mapping.

VI. Summary and Future Work

We present in this paper a joint segmentation and classification system for SAR sea-ice analysis. The segmentation algorithm is based on a region-growing technique, and the classification is a region-based MRF approach. The two processes are integrated under the Bayesian framework, with both aiming at reducing a defined energy. The interactions between the two are bidirectional by letting the classification result to have some degree of control on the region-growing process. Various low-level features and high-level knowledge can hence be efficiently combined, and the system performs successfully with the tested SAR sea-ice images.

The proposed system performs the solution searching in a bottom-up manner on the hierarchical structure established during the process. More accurate results could also be obtained with a subsequent top-down searching and adaptive updating of the structure. Also, the ice-floe-shape descriptor may be improved by a more general class of curves [48].

All experimental results are evaluated subjectively due to the difficulty of obtaining the pixel-level ground truth. The human expert interpretations agree with the experimental results. Although such an evaluation is qualitative, our system is a practical solution to the identifications of difficult ice types, such as gray ice and gray–white ice, which, to our knowledge, has not been explored before. Future works are required for quantitative evaluations.

Acknowledgment

The authors would like to thank the referees for their thoughtful and insightful reviews that helped improve the overall quality of this paper. RADARSAT images are copyrighted by the Canadian Space Agency (CSA).

References

[1] World Meteorology Organization, Dec. 17, 2005. [Online]. Available: http://www.wmo.ch/index-en.html
[2] A. Baraldi and F. Parmiggiani, "An investigation of the textural characteristics associated with gray level cooccurrence matrix statistical parameters," *IEEE Trans. Geosci. Remote Sens.*, vol. 33, no. 2, pp. 293–304, Mar. 1995.
[3] D. G. Barber and E. F. LeDrew, "SAR sea ice discrimination using texture statistics: A multivariate approach," *Photogramm. Eng. Remote Sens.*, vol. 57, no. 4, pp. 385–395, 1991.
[4] A. V. Bogdanov, M. Toussaint, and S. Sandven, "Recurrent modular network architecture for sea ice classification in the marginal ice zone using ERS SAR images," in *Proc. SPIE—Image Signal Process. Remote Sens. XI*, L. Bruzzone, Ed., Oct. 2005, vol. 5982, pp. 283–287.
[5] A. V. Bogdanov, S. Sandven, O. M. Johannessen, V. Y. Alexandrov, and L. P. Bobylev, "Multisensor approach to automated classification of sea ice image data," *IEEE Trans. Geosci. Remote Sens.*, vol. 43, no. 7, pp. 1648–1664, Jul. 2005.
[6] M. E. Shokr, "Evaluation of second-order texture parameters for sea ice classification from radar images," *J. Geophys. Res.*, vol. 96, no. C6, pp. 10 625–10 640, 1991.
[7] L. K. Soh and C. Tsatsoulis, "Texture analysis of SAR sea ice imagery using gray level cooccurrence matrices," *IEEE Trans. Geosci. Remote Sens.*, vol. 37, no. 2, pp. 780–795, Mar. 1999.
[8] D. A. Clausi and B. Yue, "Comparing cooccurrence probabilities and Markov random fields for texture analysis of SAR sea ice imagery," *IEEE Trans. Geosci. Remote Sens.*, vol. 42, no. 1, pp. 215–228, Jan. 2004.
[9] H. Deng and D. A. Clausi, "Unsupervised segmentation of synthetic aperture radar sea ice imagery using a novel Markov random field model," *IEEE Trans. Geosci. Remote Sens.*, vol. 43, no. 3, pp. 528–538, Mar. 2005.
[10] R. Samadani, "A finite mixture algorithm for finding proportions in SAR images," *IEEE Trans. Image Process.*, vol. 4, no. 8, pp. 1182–1186, Aug. 1995.
[11] L. K. Soh and C. Tsatsoulis, "Unsupervised segmentation of ERS and radarsat sea ice images using multiresolution peak detection and aggregated population equalization," *Int. J. Remote Sens.*, vol. 20, no. 15/16, pp. 3087–3109, 1999.
[12] J. A. Karvonen, "Baltic sea ice SAR segmentation and classification using modified pulse-coupled neural networks," *IEEE Trans. Geosci. Remote Sens.*, vol. 42, no. 7, pp. 1566–1574, Jul. 2004.
[13] J. Karvonen, M. Simila, and M. Makynen, "Open water detection from Baltic sea ice Radarsat-1 SAR imagery," *IEEE Geosci. Remote Sens. Lett.*, vol. 2, no. 3, pp. 275–279, Jul. 2005.
[14] P. Maillard, D. A. Clausi, and H. Deng, "Operational map-guided classification of SAR sea ice imagery," *IEEE Trans. Geosci. Remote Sens.*, vol. 43, no. 12, pp. 2940–2951, Dec. 2005.

[15] L. K. Soh, C. Tsatsoulis, D. Gineris, and C. Bertoia, "ARKTOS: An intelligent system for SAR sea ice image classification," *IEEE Trans. Geosci. Remote Sens.*, vol. 42, no. 1, pp. 229–248, Jan. 2004.
[16] S. Z. Li, *Markov Random Field Modeling in Image Analysis*. New York: Springer-Verlag, 2001.
[17] Q. Yu and D. A. Clausi, "Combining local and global features for image segmentation using iterative classification and region merging," in *Proc. 2nd Can. Conf. Comput. Robot Vis.*, Victoria, BC, Canada, May 9–11, 2005, pp. 579–586.
[18] Canadian Ice Service, Dec. 20, 2005. [Online]. Available: http://ice-glaces.ec.gc.ca
[19] J. Karvonen, M. Simila, and I. Heiler, "Ice thickness estimation using SAR data and ice thickness history," in *Proc. IEEE Int. Geosci. Remote Sens. Symp.*, 2003, vol. 1, pp. 74–76.
[20] F. D. Carsey, Ed., *Microwave Remote Sensing of Sea Ice*. Washington, DC: AGU, 1992
[21] W. Dierking and T. Busche, "Sea ice monitoring by L-band SAR: An assessment based on literature and comparisons of JERS-1 and ERS-1 imagery," *IEEE Trans. Geosci. Remote Sens.*, vol. 44, no. 4, pp. 957–970, Apr. 2006.
[22] J. S. Lee, "Speckle analysis and smoothing of SAR images," *Comput. Graph. Image Process.*, vol. 17, no. 1, pp. 24–32, 1981.
[23] V. S. Frost, J. A. Stiles, K. S. Shanmugan, and J. C. Holtzman, "A model for radar images and its application to adaptive digital filtering of multiplicative noise," *IEEE Trans. Pattern Anal. Mach. Intell.*, vol. PAMI-4, no. 2, pp. 157–166, Mar. 1982.
[24] D. T. Kuan, A. A. Sawchuk, T. C. Strand, and P. Chavel, "Adaptive restoration of images with speckle," *IEEE Trans. Acoust., Speech, Signal Process.*, vol. ASSP-35, no. 3, pp. 373–383, Mar. 1987.
[25] G. Ramponi and C. Moloney, "Smoothing speckled images using an adaptive rational operator," *IEEE Signal Process. Lett.*, vol. 4, no. 3, pp. 68–71, Mar. 1997.
[26] Y. Yu and S. T. Acton, "Speckle reducing anisotropic diffusion," *IEEE Trans. Image Process.*, vol. 11, no. 11, pp. 1260–1270, Nov. 2002.
[27] M. P. Mäkynen, A. T. Manninen, M. H. Similä, J. A. Karvonen, and M. T. Hallikainen, "Incidence angle dependence of the statistical properties of C-band HH-polarization backscattering signatures of the Baltic sea ice," *IEEE Trans. Geosci. Remote Sens.*, vol. 40, no. 12, pp. 2593–2605, Dec. 2002.
[28] R. A. Shuchman, C. C. Wackerman, A. L. Maffett, R. G. Onstott, and L. L. Sutherland, "The discrimination of sea ice types using SAR backscatter statistics," in *Proc. Geosci. Remote Sens. Symp.*, Vancouver, BC, Canada, 1989, pp. 381–385.
[29] D. A. Clausi, "An analysis of cooccurrence texture statistics as a function of grey level quantization," *Can. J. Remote Sens.*, vol. 28, no. 1, pp. 45–62, 2002.
[30] W. Yang, C. He, Y. Cao, H. Sun, and X. Xu, "Improved classification of SAR sea ice imagery based on segmentation," in *Proc. IGARSS*, Jul. 2006, pp. 3727–3730.
[31] B. A. Draper, R. T. Collins, J. Brolio, A. R. Hanson, and E. M. Riseman, "The schema system," *Int. J. Comput. Vis.*, vol. 2, no. 3, pp. 209–250, Jan. 1989.
[32] S. S. Hwang, L. S. Davis, and T. Matsuyama, "Hypothesis integration in image understanding systems," *Comput. Vis. Graph. Image Process.*, vol. 36, no. 2/3, pp. 321–371, 1986.
[33] C. E. Liedtke, J. Bückner, O. Grau, S. Growe, and R. Tönjes, "AIDA: A system for the knowledge based interpretation of remote sensing data," in *Proc. 3rd Int. Airborne Remote Sens. Conf. Exhib.*, Copenhagen, Denmark, Jul. 1997, vol. 2, pp. 313–320.
[34] H. Niemann, G. F. Sagerer, S. Schroder, and F. Kummert, "Ernest: A semantic network system for pattern understanding," *IEEE Trans. Pattern Anal. Mach. Intell.*, vol. 12, no. 9, pp. 883–905, Sep. 1990.
[35] J. W. Modestino and J. Zhang, "A Markov random field model based approach to image interpretation," *IEEE Trans. Pattern Anal. Mach. Intell.*, vol. 14, no. 6, pp. 606–615, Jun. 1992.
[36] J. Pearl, *Probabilistic Reasoning in Intelligent Systems: Networks of Plausible Inference*. San Mateo, CA: Morgan Kaufmann, 1988.
[37] Q. Yu, "Automated SAR sea ice interpretation," Ph.D. dissertation, Dept. Syst. Design Eng., Univ. Waterloo, Waterloo, ON, Canada, 2006.
[38] J. Besag, "Spatial interaction and the statistical analysis of lattice systems," *J. R. Stat. Soc., Ser. B*, vol. 36, no. 2, pp. 192–236, 1974.
[39] H. Derin and H. Elliott, "Modeling and segmentation of noisy and textured images using Gibbs random fields," *IEEE Trans. Pattern Anal. Mach. Intell.*, vol. PAMI-9, no. 1, pp. 39–55, Jan. 1987.
[40] C. S. Won and H. Derin, "Unsupervised segmentation of noisy and textured images using Markov random fields," *CVGIP, Graph. Models Image Process.*, vol. 54, no. 4, pp. 308–328, 1992.
[41] L. Vincent and P. Soille, "Watershed in digital spaces: An efficient algorithm based on immersion simulations," *IEEE Trans. Pattern Anal. Mach. Intell.*, vol. 13, no. 6, pp. 583–598, Jun. 1991.
[42] J. A. Feldman and Y. Yakimovsky, "Decision theory and artificial intelligence I: Semantics-based region analyzer," *Artif. Intell.*, vol. 5, no. 4, pp. 349–371, 1974.
[43] M. Sonka, V. Hlavac, and R. Boyle, *Image Processing, Analysis, and Machine Vision*. Boston, MA: Thomson Course Technology, 1998.
[44] A. Barbu and S. C. Zhu, "Generalizing Swendsen-Wang to sampling arbitrary posterior probabilities," *IEEE Trans. Pattern Anal. Mach. Intell.*, vol. 27, no. 8, pp. 1239–1253, Aug. 2005.
[45] M. K. Hu, "Visual pattern recognition by moment invariants," *IRE Trans. Inf. Theory*, vol. 8, no. 2, pp. 179–187, 1961.
[46] R. O. Duda, P. E. Hart, and D. G. Stork, *Pattern Classification*. Hoboken, NJ: Wiley, 2001.
[47] I. Y. Kim and H. S. Yang, "An integration scheme for image segmentation and labelling based on Markov random field model," *IEEE Trans. Pattern Anal. Mach. Intell.*, vol. 18, no. 1, pp. 69–73, Jan. 1996.
[48] J. Banfield, "Automated tracking of ice floes: A stochastic approach," *IEEE Trans. Geosci. Remote Sens.*, vol. 29, no. 6, pp. 905–911, Nov. 1991.

Qiyao Yu received the B.A.Sc. degree from Tsinghua University, Beijing, China, in 1997, the M.A.Sc. degree from the Memorial University of Newfoundland, St. John's, NF, Canada, in 2002, and the Ph.D. degree in systems design engineering from the University of Waterloo, Waterloo, ON, Canada, in 2006.

He is currently with Eutrovision Inc., Shanghai, China. His research interest is in image and video processing, pattern recognition, and remote sensing.

David A. Clausi (S'93–M'96–SM'03) received the B.A.Sc., M.A.Sc., and Ph.D. degrees in systems design engineering from the University of Waterloo, Waterloo, ON, Canada, in 1990, 1992, and 1996, respectively.

After completing his doctorate, he worked in the medical imaging field with Mitra Imaging Inc., Waterloo. He started his academic career in 1997 as an Assistant Professor in geomatics engineering with the University of Calgary, Calgary, AB, Canada. In 1999, he returned to the University of Waterloo and was awarded tenure and promotion to Associate Professor in 2003, where he is currently with the Department of Systems Design Engineering. He is an active Interdisciplinary and Multidisciplinary Researcher. He has an extensive publication record, publishing refereed journal and conference papers in diverse fields of remote sensing, computer vision, algorithm design, and biomechanics. His primary research interest is automated interpretation of synthetic aperture radar sea-ice imagery in support of the operational activities of the Canadian Ice Service. The research results have successfully led to commercial implementations.

Dr. Clausi has received numerous scholarships, conference paper awards, and two Teaching Excellence Awards.